Time-resolved tomography using acoustic emissions in the laboratory, and application to sandstone compaction

Nicolas Brantut

Rock and Ice Physics and Seismological Laboratory, Department of Earth Sciences, University College London, London WC1E6BT, UK.
E-mail: n.brantut@ucl.ac.uk

SUMMARY

Acoustic emission (AE) and active ultrasonic wave velocity monitoring are often performed during laboratory rock deformation experiments, but are typically processed separately to yield homogenized wave velocity measurements and approximate source locations. Here, I present a numerical method and its implementation in a free software to perform a joint inversion of AE locations together with the 3-D, anisotropic *P*-wave structure of laboratory samples. The data used are the *P*-wave first arrivals obtained from AEs and active ultrasonic measurements. The model parameters are the source locations and the *P*-wave velocity and anisotropy parameter (assuming transverse isotropy) at discrete points in the material. The forward problem is solved using the fast marching method, and the inverse problem is solved by the quasi-Newton method. The algorithms are implemented within an integrated free software package called FaATSO (**Fa**st Marching **A**coustic Emission **T**omography using **S**tandard **O**ptimisation). The code is employed to study the formation of compaction bands in a porous sandstone. During deformation, a front of AEs progresses from one end of the sample, associated with the formation of a sequence of horizontal compaction bands. Behind the active front, only sparse AEs are observed, but the tomography reveals that the *P*-wave velocity has dropped by up to 15 per cent, with an increase in anisotropy of up to 20 per cent. Compaction bands in sandstones are therefore shown to produce sharp changes in seismic properties. This result highlights the potential of the methodology to image temporal variations of elastic properties in complex geomaterials, including the dramatic, localized changes associated with microcracking and damage generation.

Key words: Fracture and flow; Microstructure; Tomography; Acoustic properties; Seismic tomography; Dynamics and mechanics of faulting.

1 INTRODUCTION

In situ imaging of samples during laboratory rock deformation experiments is crucial for our understanding of the physics of deformation and strain localization in rocks. However, the elevated pressures and temperatures required to perform relevant experiments generally preclude direct observation techniques. Since the 1960s, *in situ* acoustic emission (AE) monitoring techniques have been developed to detect microfracture propagation and extract event locations, amplitudes and focal mechanisms (e.g. Mogi 1968; Scholz 1968; Nishizawa *et al.* 1984; Lockner 1993); such observations have revealed unprecedented details about the dynamics of fault growth (Lockner *et al.* 1992) and strain localization in crustal rocks (e.g. Fortin *et al.* 2009). Passive AE monitoring is only able to record the microcracks that propagate dynamically and generate elastic waves within the frequency and amplitude range of the recording devices. Therefore, passive AE monitoring can be usefully complemented by active measurements of *P*- and *S*-wave velocities, which provide

unique information on the development of seismic anisotropy (e.g. Gupta 1973; Lockner & Byerlee 1977) and on the evolution of microfracture density and orientation (e.g. Sayers & Kachanov 1995; Schubnel *et al.* 2003) during rock deformation experiments.

Despite the great advances in *in situ* imaging made possible by AE and ultrasonic monitoring, both methods rely on the key simplifying assumption that the elastic wave velocities remain homogeneous throughout the material. Indeed, AE locations are determined by assuming a homogeneous, possibly anisotropic velocity structure and the active measurements of *P*- and *S*-wave velocities are made between pairs of sensors assuming straight ray paths, effectively corresponding to path-averaged velocities. However, it is well known that strong structural heterogeneities often develop in rock samples during deformation experiments, especially in the brittle regime where strain and microcrack damage localize along a fault plane. We expect these strain and damage heterogeneities to be associated with sharp local changes in elastic wave velocities and anisotropy, by up to several tens of percent (e.g. Schubnel

2177

et al. 2003; Fortin *et al.* 2006; Brantut *et al.* 2014). The development of a complex wave velocity structure in the material has two consequences. First, if not properly accounted for, it severely limits the accuracy of AE locations. Secondly, and perhaps most importantly, the wave velocity structure becomes a key signature of the deformation processes operating in the material. It is therefore tempting to aim to determine a tomographic picture of the velocity structure, using AE and/or ultrasonic data.

In order to achieve this, the most natural starting point is to use active measurements with known source positions. Using this type of data, Yukutake (1989), Falls *et al.* (1992) and Jansen *et al.* (1993) were able to retrieve 2-D tomographic sections of rock samples subjected to shear, thermal and hydraulic stresses, respectively. In all cases, the array of transducers was quite extensive, the rock samples were quite large (more than 10 cm in width) and not positioned inside a pressure vessel. Furthermore, the tomographic reconstruction algorithm assumed straight ray paths (Dines & Lytle 1979). In addition to the limitation imposed by the latter hypothesis when strong (more than 10 per cent) velocity contrasts develop, the method used by Falls *et al.* (1992) and Jansen *et al.* (1993) is not easily extendable to 3-D tomography, which would require a much larger number of sensors to provide a reasonable ray coverage of the samples. Due to space and sample size limitations, typical triaxial deformation apparatus are equipped with only 10–20 piezoelectric transducers, thus making purely active tomography impossible in practice (see Brantut 2010, section 8.9).

Here, I present a method that combines both active ultrasonics and passive AE monitoring data to improve the ray coverage in laboratory samples, and achieve jointly 3-D, anisotropic tomographic reconstruction and improved AE event location. During brittle failure or cataclastic flow experiments, the number of AE events is several orders of magnitude larger than the number of active transducers; furthermore, the AE locations are by definition more widely distributed (even though they often become clustered when strain localizes) than the fixed positions of the sensors. Therefore, the key idea is to use the AE events as passive sources in order to increase dramatically the ray coverage of the sample. Unfortunately, this major advantage comes with a significant cost: the determination of the AE source locations becomes coupled to the determination of the velocity structure. In other words, one cannot simply assume that the AE locations are known exactly, so that they become part of the inverse problem. Translated into the language of inverse problems, the observed data **d** are the arrival times measured from active and passive recordings, and the model parameters **m** are the wave velocities and anisotropy parameters at discretized points in space within the material, together with the source locations of all AE events. The physical model employed to make predictions of **d** based on known parameters **m**,

$$\mathbf{d} = \mathbf{g}(\mathbf{m}), \tag{1}$$

is an eikonal solver **g**.

The principle of this approach is not new. It is essentially similar to Local Earthquake Tomography, a method developed in seismology to determine local velocity structures and accurate earthquake locations in seismically active regions (Aki & Lee 1976; Thurber 1983). However, the use and implementation of the technique in a laboratory setting presents several important challenges. The most prominent one is the efficient computation of theoretical arrival times (the forward problem) in three dimensions, including anisotropy and with the capability of handling strong contrasts. This combination of features is rarely required in seismological studies, and it was therefore deemed necessary to implement a specific method that could handle it. The subsequent key step is to com-

pute the sensitivity of the arrival times with respect to the inversion parameters: velocity and anisotropy in the material, as well as source locations. Here again, a specific method using posterior ray tracing and trilinear interpolation was developed to perform this step efficiently. One other specifics of the laboratory studies is that the array of piezoelectric transducers is used for both passive and active measurements (whereby they act as ultrasonic sources as well as receivers). It is therefore important to include both types of data, and to accurately include their different range of measurement errors (i.e. variances and covariances on **d** and **m**). The very large number of AE events typically observed during brittle failure or cataclastic deformation of rocks (at least several thousand events) is a great advantage in terms of data coverage, but imposes the need to use automatic *P*-wave arrival time picking techniques which are never perfect. The challenge here is to achieve accurate picking of a majority of waveforms, while selectively rejecting bad picks to avoid including outliers with large errors in the inversion scheme.

Taken together, the specifics associated with using laboratory data call for the development of a specialized computational tool to perform what could be called 'Local Acoustic Emission Tomography'. In this paper, I present a set of methods and their implementation into an integrated free software called FaATSO (acronym for **Fa**st Marching **A**coustic Emission **T**omography using **S**tandard **O**ptimisation) that performs 3-D, anisotropic AE tomography. The code is based on two key algorithms: (1) the fast marching method (Sethian 1999), employed to solve the forward problem, and (2) the quasi-Newton method (e.g. Tarantola 2005), used to solve the inverse problem. The software package is written in C++ with Matlab wrappers, and released online (under a free license, GNU GPL version 3) at https://github.com/nbrantut/Faatso.git. The performance and potential applications of the method are demonstrated on experimental data obtained during compactant deformation of a porous sandstone.

The paper is organized as follows. In Section 2, I describe the fast marching method and its implementation for a simple case of elliptical anisotropy relevant to most rock deformation experiments. Section 3 presents the quasi-Newton method to solve the inverse problem, and a particular emphasis is placed on the subtleties associated with the determination of ray paths and sensitivity kernels. A complete application of the method for a sandstone compaction experiment is given in Section 4. Conclusions and perspectives are presented in Section 5.

2 FORWARD PROBLEM: 3-D FAST MARCHING METHOD WITH ELLIPTICAL ANISOTROPY

A wide variety of numerical methods exist to compute arrival times of seismic (or acoustic) waves in complex media (e.g. Rawlinson & Sambridge 2003). Because of the strong heterogeneities expected in laboratory samples, a natural choice is to use methods based on full wave front propagation rather than ray tracing. One of the most computationally efficient algorithms to compute wave fronts in strongly heterogeneous media is the fast marching method, which has been developed to solve so-called 'viscosity' solutions of Hamilton–Jacobi equations; a class of partial differential equations that includes the eikonal equation for seismic traveltimes (see review in Sethian 1999). The key benefit of the fast marching method is its unconditional stability, regardless of the velocity heterogeneity encountered by the wave front. Furthermore, wave front tracking is also beneficial because a single computation yields arrival times at many possible receivers from a given source. In this section, I

briefly recall the principle of the method and explain the key implementation details for transversely isotropic media with vertical axis of symmetry (VTI).

2.1 Principle

For an anisotropic medium, the eikonal equation reads:

$$\sqrt{(\partial_x u)^2 + (\partial_y u)^2 + (\partial_z u)^2} \times V\left(\mathbf{x}; \frac{\nabla u}{|\nabla u|}\right) = 1, \tag{2}$$

where u is the wave front arrival time, $\mathbf{x} = (x, y, z)$ denotes Cartesian coordinates and V is the wave speed, which depends on the position and the orientation of the wave front. For VTI materials, the phase velocity is entirely determined by the phase angle θ, which is the angle between the direction normal to the wave front and the vertical direction.

A discretized version of eq. (2) using *upwind* first-order finite differences on a regular Cartesian grid is due to Rouy & Tourin (1992):

$$\left\{ \max(D_{ijk}^{-x}u, -D_{ijk}^{+x}u, 0)^2 + \max(D_{ijk}^{-y}u, -D_{ijk}^{+y}u, 0)^2 \right.$$
$$\left. + \max(D_{ijk}^{-z}u, -D_{ijk}^{+z}u, 0)^2 \right\}^{1/2} \times V_{ijk}(\theta) = 1, \tag{3}$$

where $V_{ijk}(\theta)$ is the wave velocity at node (i, j, k), and

$$D_{ijk}^{\pm x}u = \frac{u_{i,j,k} - u_{i\pm 1,j,k}}{h} \tag{4}$$

denote first-order finite-difference operators, where h is the (uniform) grid spacing.

The fast marching method consists in solving eq. (3) sequentially, from small to large values of u, hence progressively advancing the wave front. The use of *upwind* finite differences is absolutely key: it allows the preservation of causality and ensures the unconditional stability of the method (if first-order finite differences are used). A discussion and proof of why this holds is given in Sethian (1999). The method was originally developed for *isotropic* eikonal equations, but can also be applied for *anisotropic* equations without modification in special cases (further details below). The algorithm is the following:

(i) Fix the starting source point at $u = 0$, and tag this point *known*, all other points begin tagged as *unknown*.

(ii) Update the neighbours of the newly *known* point by solving eq. (3), and tag them *trial* and remove them from the *unknown* set.

(iii) Choose the point with minimum u among the *trial* points, tag it as *known* and remove it from the *trial* set.

(iv) Go back to (ii), until no points remain tagged as *trial*.

The key step is (iii), which ensures that points are updated with increasing values of u (the information does not flow backwards). The computational efficiency of the method relies on the storage of the *trial* points in a so-called 'min-heap' data structure (in FaATSO, a Fibonacci heap from the C++ Boost library is used), so that the *trial* point with minimum arrival time is always at the top of the heap, and the addition of *trial* points and reordering of the heap is performed more efficiently than with conventional sorting algorithms.

2.2 Anisotropy

In case of VTI materials, the velocity is only dependent on the angle θ between the vertical axis and the direction of the normal to the wave front. In this work, I use a simple elliptical anisotropy:

$$V(\theta) = V_0(1 + E\cos^2 \theta), \tag{5}$$

parametrized with the horizontal wave velocity, V_0, and the relative excess in vertical wave velocity E. The parameter E is related to Thomsen's parameter ϵ:

$$E = -\frac{\epsilon}{1 + \epsilon}, \tag{6}$$

assuming a model for weak anisotropy and $\delta = \epsilon$ (Thomsen 1986). In this model, $V(\theta)$ is the phase velocity and θ is the phase angle. The cosine of θ is related to the partial derivatives of u in the following way:

$$\cos\theta = \frac{\partial_z u}{\sqrt{(\partial_x u)^2 + (\partial_y u)^2 + (\partial_z u)^2}}. \tag{7}$$

Although the fast marching method requires some modifications for general anisotropy (e.g. Sethian & Vladimirsky 2003), it can be shown that the conventional method as outlined above is valid when the direction of anisotropy is aligned with the grid and the anisotropy is not too strong. This is the case here provided that $-1/2 < E < 1$ (see Appendix A), which is largely in the remit of the approximation of weak anisotropy.

In practice, the assumption of VTI geometry is particularly relevant to initially isotropic rock samples subjected to triaxial compression in the laboratory. Indeed, loading under triaxial conditions tend to generate stress- and crack-induced anisotropies aligned with the compression axis (Paterson & Wong 2005, see also Section 4).

2.3 Second-order finite differences

The first-order finite-difference approximation of the eikonal equation is quite crude, and tends to generate large errors along diagonal points of the grid (e.g. Rickett & Fomel 1999). This can be mitigated by using a second-order (upwind) approximation, as described in Sethian (1999). The discretized eikonal equation becomes:

$$\left\{ \max\left[D_{ijk}^{-x}u + s_{ijk}^{-x}D_{ijk}^{-2x}u, -D_{ijk}^{+x}u + s_{ijk}^{+x}D_{ijk}^{+2x}u, 0 \right]^2 \right.$$
$$+ \max\left[D_{ijk}^{-y}u + s_{ijk}^{-y}D_{ijk}^{-2y}u, -D_{ijk}^{+y}u + s_{ijk}^{+y}D_{ijk}^{+2y}u, 0 \right]^2$$
$$+ \max\left[D_{ijk}^{-z}u + s_{ijk}^{-z}D_{ijk}^{-2z}u, -D_{ijk}^{+z}u + s_{ijk}^{+z}D_{ijk}^{+2z}u, 0 \right]^2 \Big\}^{1/2}$$
$$\times V_{ijk}(\theta) = 1, \tag{8}$$

where $s_{i,j,k}$ are switches defined by

$$s_{ijk}^{\pm x} = \begin{cases} 1 & \text{if } u_{i\pm 2,i,k} \text{ and } u_{i\pm 1,i,k} \text{ are known} \\ & \text{and } u_{i\pm 2,i,k} < u_{i\pm 1,j,k}, \\ 0 & \text{otherwise,} \end{cases} \tag{9}$$

and

$$D_{ijk}^{\pm 2x}u = \frac{u_{i,j,k} - 2u_{i\pm 1,j,k} + u_{i\pm 2,j,k}}{2h}. \tag{10}$$

One important fact to keep in mind when using a second-order approximation is that the scheme may not be applicable when sharp changes in wave speeds occur. In that case, the solution of $u_{i,j,k}$ might not exist (or would be a complex number), and we have to revert to the first-order scheme [eq. (3)].

2.4 Ray tracing

Once the arrival times have been computed at all points, it is relatively easy to compute ray paths a posteriori. In the isotropic case, ray tracing is straightforward because the ray angle at every point
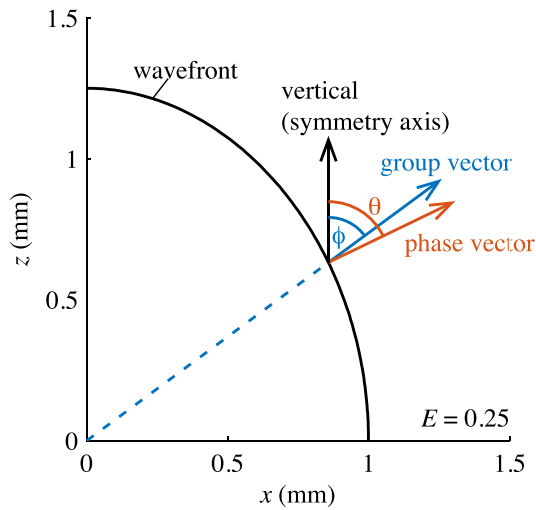
Figure 1. Illustration of the difference between the phase (red) and group (blue) angles for a wave front propagating in a homogeneous material with $E = 0.25$.

is perpendicular to the wave front (i.e. following the gradient of the arrival time field). In the anisotropic case, the situation is somewhat different because the rays are no longer perpendicular to the wave front: the phase angle is not the same as the group angle. So, at every point, one needs to compute the group angle (from the phase angle, given by the gradient of the arrival time field) in order to obtain the ray orientation.

The relationship between group velocity V_{group} and phase velocity V is (Thomsen 1986):

$$V_{group}^2(\phi) = V^2(\theta) + \left(\frac{dV}{d\theta}\right)^2, \tag{11}$$

where ϕ is the group angle and θ is the phase angle. The relationship between the group and the phase angles is:

$$\tan\phi = \frac{\tan\theta + (1/V)(dV/d\theta)}{1 - (\tan\theta/V)(dV/d\theta)}. \tag{12}$$

Here, the phase velocity is given by

$$V(\theta) = V_0(1 + E\cos^2\theta). \tag{13}$$

Therefore, the group angle is then given by

$$\tan\phi = \tan\theta \frac{1 - E + \tan^2\theta}{1 + E + (1 + 2E)\tan^2\theta}, \tag{14}$$

and the group velocity is (as a function of the *phase* angle θ)

$$V_{group}[\phi(\theta)] = V_0 \times F(\theta, E), \tag{15}$$

where

$$F(\theta, E) = \left\{1 + 2E\cos^2\theta + E^2\cos^2\theta\left(1 + 3\sin^2\theta\right)\right\}^{1/2}. \tag{16}$$

Fig. 1 provides an illustration of the differences between group and phase angles for an anisotropy parameter of $E = 0.25$. In practice, the rays are traced from the receivers to the source by successively generating piecewise linear segments oriented according to the local group angle as computed from eq. (14). The segment length is chosen to be equal to the grid spacing.
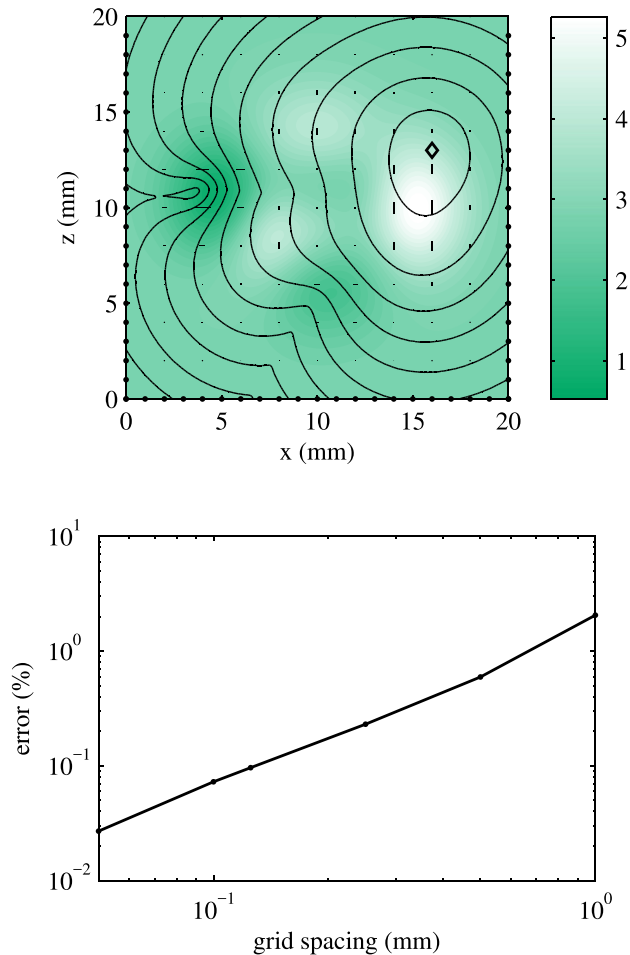
2.5 Accuracy

Strictly speaking, the finite-difference scheme is not globally second-order accurate, because the conditions for the switches are not always met. This is usually quite benign, except for the points immediately surrounding the source node: this is where the error is the largest, especially along the diagonals, because there is no way to use a second-order scheme around the source. Therefore, if used as is, the large first-order error generated around the source node will be 'dragged' along throughout the grid, even if second-order approximations are made after that. This is illustrated in Figs 2 (a) and (b), which show a very large error of the fast marching method results (up to 20 per cent) along the diagonal points near the source region. A way around this issue can be found in Rickett & Fomel (1999), and consists of computing arrival times immediately around the source node analytically, assuming a constant velocity (and anisotropy) there. This 'source box' is made large enough to include all the eight nearest points within a cube surrounding the source, and especially includes all the first diagonal points. The improvement resulting from this technique is illustrated in Fig. 2(c), which shows a significant reduction of the error near the source region and throughout the medium (less than 5 per cent) when the source box is used compared to when it is not.

The overall accuracy of the numerical scheme is explored in Fig. 3, where a complex heterogeneous and anisotropic velocity
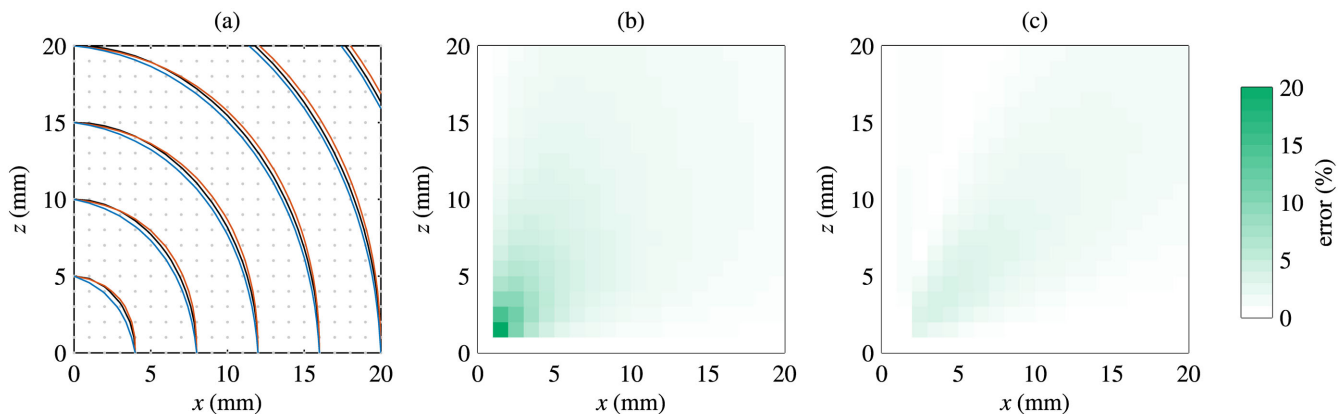
Figure 2. Accuracy of the second-order finite-difference scheme used in the fast marching method for a homogeneous, anisotropic case. (a) Contours of computed arrival times using the analytical solution (black) and the fast marching method with (red) and without (blue) a source box. The horizontal wave velocity is $V_0 = 1$ mm μs^{-1} and the anisotropy parameter is $E = 0.25$. The medium is discretized in an array of 21×21 nodes. Relative errors are shown for the case without (b) and with (c) the source box.

Figure 3. Accuracy and convergence of the fast marching method in a complex heterogeneous and anisotropic medium. The top panel shows the heterogeneity in V_0 (horizontal wave speed) and E (anisotropy). The direction and intensity of anisotropy is displayed as thin black lines. The position of the source is given by the black diamond, and the successive wave front positions are shown as black contours. The bottom panel shows the average relative error in arrival times recorded at virtual stations (shown as black dots in the top panel) as a function of grid spacing, where a model with a grid spacing of 0.02 mm was used as reference.

structure is used. Due to the strong heterogeneities, with V_0 ranging from 0.5 to 5.5 mm µs^{-1} and E ranging from -0.32 to $+0.40$, the wave front deviates from circularity and becomes cuspate in the low-velocity zone. The relative error in arrival time at receivers positioned on the boundary of the model (displayed as black dots) is computed as a function of grid spacing from 0.05 to 1 mm (i.e. from 401 to 21 gridpoints in each direction). In the absence of a true analytical solution for this velocity structure, a model with grid spacing of 0.02 mm (1001 points) is used for reference. The average error ranges from around 2 per cent in the coarsest grid, down to 0.03 per cent in the finest grid. The error decreases linearly with decreasing step size, indicating that the numerical method is globally of first order; this is not surprising considering that switches (eq. 8) are not always activated.

The computation times are remarkably short, from around 0.001 s in the 21 × 21 grid to 1.75 s in the 1001 × 1001 grid on a laptop using a single core of a 2.8 GHz Intel i7 processor. The speed of computation does not depend on the model complexity, but computations are moderately faster in the absence of anisotropy. As explained below, a grid made of around 1 million nodes is a con-

venient choice in practice to achieve computations in a reasonable timescale.

2.6 Applicability and limitations

The computation of arrival times is performed by solving the eikonal equation, which is a high-frequency approximation of the wave equation. Therefore, there are several limitations to bear in mind regarding the applicability and physical resolution expected when using this technique to simulate laboratory observations.

In laboratory studies, AEs and ultrasonic data are often recorded using uncalibrated, resonant piezoelectric transducers the characteristics of which are given by the piezoelectric properties and dimensions of the transducer and casing. The resonant frequency of typical transducers is of the order of 1 MHz, which is characteristic of lead–zirconate–titanate ceramic discs of 1–2 mm in thickness and 4–5 mm in diameter. In a rock where the P-wave velocity is 5 mm µs^{-1}, the wavelength of the signals is of the order of 5 mm. The eikonal approximation is only valid if spatial variations in velocity occur over length scales significantly larger than the wavelength, which imposes a physical lower bound on the spatial resolution of the velocity model. Any wave velocity variations occurring over length scales smaller than the signal wavelength, that is, around 5 mm, will be averaged out, and may produce scattering.

In practice, AE and ultrasonic monitoring is typically performed using laboratory samples of 4–10 cm in diameter and 8–20 cm in length, so that the high-frequency approximation is often justified.

The extension of the method to finite frequencies would require the computation of the full wavefield to solve the forward problem, which is dramatically more computationally expensive than the computation of high-frequency wave fronts. Recent advances towards understanding waveform records from active measurements (e.g. Fukushima *et al.* 2009; Yoshimitsu *et al.* 2016) show that the radiation patterns from piezoelectric transducers (see Tang *et al.* 1994) and the cylindrical geometry introduce significant complexity in the transmitted signals and enhance the measurement errors. Such measurement errors, as well as the imperfection of the forward problem itself, can be accounted for in the formulation of the inverse problem (see below).

3 INVERSE PROBLEM

3.1 Assumptions and prior information

The fast marching method is an efficient tool to compute arrival times throughout a material based on a known velocity structure and source position. The data set used for tomography consists of arrival times from both active and passive sources. In typical laboratory experiments, the number of AE events (hereafter denoted n_{evt}) is much larger than the number of transducers (denoted n_{chan}). Taking advantage of the reciprocity of the wave equation, it is sufficient to compute arrival times using the transducers as sources and collect the arrival times at the positions of the events. The same set of transducers is often used as sources in the active measurements, so that there are up to $n_{chan} \times (n_{chan} - 1 + n_{evt})$ arrival times. In practice, not all arrivals can be accurately picked on all channels, so that the actual quantity of data is somewhat reduced.

As stated previously, the model parameters are the values of V_0 and E throughout the material, and the source locations. The material is discretized into nodes along an orthonormal grid, with the $z-$axis being the vertical direction. The choice of the number of

nodes is dictated by several constraints. From a physical point of view, the size of heterogeneities sensed by elastic waves is limited by their wavelength. In laboratory rock deformation experiments, the signal frequency is of the order of 0.5–1 MHz, so that the wavelength is of the order of several millimetres. Instead of using a relatively coarse discretization with independent nodes, here a much finer grid is used but with a correlation between neighbouring nodes over a fixed length scale. This length scale is at least commensurate to the wavelength of the signal used to probe the system, but can be adapted to the known type of heterogeneity of the material (Tarantola 2005). Furthermore, the use of a fine grid would also enhance the accuracy of the forward model computations. However, it is also desirable to limit the quantity of unknowns (especially since they are correlated) in order to ease the numerical computation and linear algebra involved in the determination of the solution (see the details below). Here, these contradictory requirements are met by using a relatively coarse grid to define the model parameters, and by refining it with trilinear interpolation when computing the forward problem. This approach allows us to minimize the number of parameters while retaining good accuracy in the computation of arrival times.

Typical cylindrical laboratory samples of 40 mm in diameter and 100 mm in length are discretized with an initial grid spacing of 5 mm and a refinement factor of 8, thus yielding around 2800 nodes (including additional grid steps outside the region of interest) in the coarse grid and more than 1.4 million nodes in the refined grid.

Due to the large number of unknowns (several thousands) and the computational cost of forward modeling, the inverse problem is not easily solved by grid search or Monte Carlo sampling methods, and we have to resort to least-squares optimization techniques. In this context, all observational errors and *a priori* information on model parameters are assumed to be described by Gaussian statistics.

The observed data (arrival times) vector is denoted $\mathbf{d}_{\text{obs}}$. The covariance matrix on the data, $\mathbf{C}_D$, is assumed to be diagonal (i.e. the observations are independent from each other). The diagonal elements of $\mathbf{C}_D$ correspond to the variances on the observed arrival times. These variances are effectively the estimated errors on the observations. The passive and active measurements do not have the same errors, and two distinct variances are introduced: one for active survey data σ_{shot}^2, and one for the passive AE arrival time data σ_{evt}^2. The latter is typically larger than the former, since the active survey arrival times can be picked very accurately using cross-correlation methods on very clear waveforms, whereas AE arrival times are picked automatically and just manually checked. In general, it would be preferable to associate each arrival time with a specific error, for instance using the information provided by the autopicking algorithm. Such a method would require further developments that are beyond the scope of this work, so here I have used a single value of σ_{evt} for all measurements.

In the framework of probabilistic inverse problems, the intrinsic error on the theory (here the ray approximation) can also be accounted for (Tarantola 2005, section 1.3). In practice, this is done by adding an additional variance on the data, that is, increasing the observational errors to include the possibility that systematic errors can be made due to the imperfection of the theory even if the observations are perfect.

The vector of *a priori* model parameters is denoted $\mathbf{m}_{\text{prior}}$. The prior information is also assumed to be Gaussian. Because the wave velocity is a strictly positive parameter [or a so-called Jeffreys parameter, see Tarantola (2005)], the logarithm of V_0 is used as the corresponding Cartesian parameter. All other parameters (anisotropy and source positions) are Cartesian. The covariance matrix in the

model space $\mathbf{C}_M$ is determined by: the variance σ_v^2 and covariances on $\ln(V_0)$, the variance σ_E^2 and covariances on E and the variances $\sigma_x^2, \sigma_y^2, \sigma_z^2$ and σ_{t0}^2 on source locations (I assume no covariance between source location parameters). The covariances on $\ln(V_0)$ and E between two nodes of indices i and j follow a 3-D exponential covariance:

$$c_{ij} = \sigma^2 \exp\left(-\frac{\sqrt{(x_i - x_j)^2 + (y_i - y_j)^2 + (z_i - z_j)^2}}{\lambda}\right), \quad (17)$$

where (x_i, y_i, z_i) are the coordinates of node i, σ^2 is the variance on either $\ln(V_0)$ or E and λ is a correlation length. Essentially, the length λ provides a smoothness of the velocity structure, preventing (statistically) heterogeneities over length scales smaller than λ.

In summary, the covariance matrix $\mathbf{C}_M$ is block diagonal, the first block being the c_{ij} for the logarithm of the velocity, the second block is the c_{ij} for the anisotropy parameter and the remaining block is a simple diagonal containing the sequence of variances on source locations.

The inverse problem is non-linear: the function $\mathbf{g}(\mathbf{m})$ in eq. (1) effectively contains integrals of slownesses over ray paths between sources and receiver. The tomographic problem is only weakly non-linear, while the source location problem is strongly non-linear. Because a Gaussian model is assumed for all parameters, it is essential that the *a priori* source locations are not too far from the true ones. In practice, initial source locations are determined using straight ray paths and an average *P*-wave velocity model (possibly anisotropic if needed).

3.2 Quasi-Newton algorithm

The method chosen to determine the mean posterior model parameters (i.e. the 'best' model in the sense of the least-squares norm) is the quasi-Newton method. It is an iterative quadratic minimization method, described in detail in Tarantola (2005, p. 78). The model parameters $\mathbf{m}$ are updated at each iteration n as

$$\mathbf{m}_{n+1} = \mathbf{m}_n - \mu_n \left(\mathbf{G}_n^t \mathbf{C}_D^{-1} \mathbf{G}_n + \mathbf{C}_M^{-1}\right)^{-1} \left(\mathbf{G}_n^t \mathbf{C}_D^{-1}(\mathbf{d}_n - \mathbf{d}_{\text{obs}})\right.$$
$$\left. + \mathbf{C}_M^{-1}(\mathbf{m}_n - \mathbf{m}_{\text{prior}})\right), \quad (18)$$

where $\mathbf{d}_n = \mathbf{g}(\mathbf{m}_n)$ and $\mu_n \approx 1$ is the step size. The matrix $\mathbf{G}_n$ contains the derivatives of $\mathbf{g}$:

$$(\mathbf{G}_n)_{ij} = \left(\frac{\partial g_i}{\partial m_j}\right)_{\mathbf{m}_n}. \quad (19)$$

In terms of implementation, the linear algebra operations in eq. (18) are performed using the C++ Armadillo package (Sanderson & Curtin 2016). Only the inverse of $\mathbf{C}_M$ and $\mathbf{C}_D$ are found explicitly, and a linear system is solved at every step instead of computing the inverse of $\left(\mathbf{G}_n^t \mathbf{C}_D^{-1} \mathbf{G}_n + \mathbf{C}_M^{-1}\right)$.

The key difficulty in the inversion procedure is computing $\mathbf{G}_n$.

3.3 Computing the matrix of derivatives

The (vector) function $\mathbf{g}$ maps the velocity structure and source locations to the arrival times at each receiver. If we denote t_{ij}, the arrival time at receiver j from source i, the mapping $\mathbf{d} = \mathbf{g}(\mathbf{m})$ can be written as

$$t_{ij} = t_0 + \int_{\mathcal{R}_{ij}} (1/V_{\text{group}}) ds, \quad (20)$$

where t_0 is the origin time of the source, $\mathcal{R}_{ij}$ is the ray path between source and receiver, s is the curvilinear coordinate along the ray
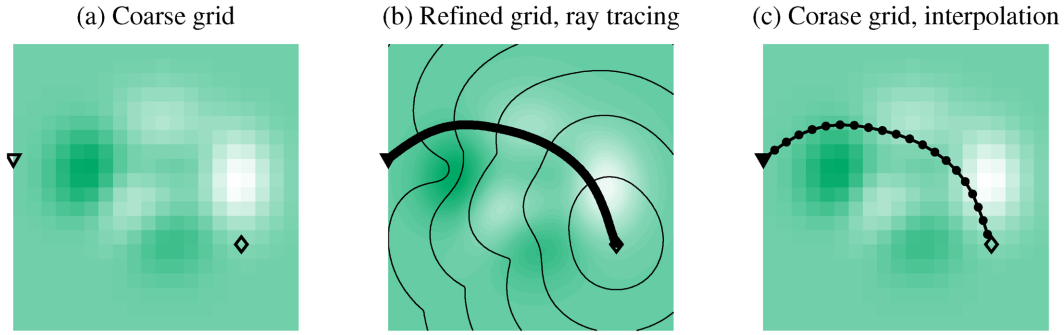
Figure 4. Ray tracing and interpolation procedure. The initial coarse velocity structure is shown in panel (a). This model is refined by trilinear interpolation (here by a factor 10), and the arrival times are computed [thin black lines in panel (b)]. The ray is traced in this refined grid [thick line in panel (b)], and the derivatives are computed with respect to the parameters as defined in the refined grid. In a final step [panel (c)], the derivatives with respect to the parameters defined in the coarse grid are determined by using the grid interpolation coefficients [eq. (37)].

path and V_{group} is the *group* velocity along the ray. The medium we are dealing with is VTI, so that the group velocity depends on the local group angle ϕ between the ray and the vertical axis. The group velocity is expressed as

$$V_{\text{group}}[\phi(\theta)] = V_0 \times F(\theta, E), \tag{21}$$

where θ is the phase angle, easily computed and stored during the ray tracing process, and F is given by eq. (16). Denoting $v = \ln(V_0)$, Eq. (20) is rewritten as

$$t_{ij} = t_0 + \int_{\mathcal{R}_{ij}} e^{-v}/F[\theta(\phi), E]ds, \tag{22}$$

and its discretized form is then

$$t_{ij} \approx t_0 + \sum_{k=0}^{N} e^{-v_k}/F(\theta_k, E_k)\Delta s_k, \tag{23}$$

where the summation is performed over all the indices $k = 0, \ldots, N$ of the segments of length Δs_k forming the ray $\mathcal{R}_{ij}$.

The derivatives are therefore:

$$\frac{\partial t_{ij}}{\partial t_0} = 1, \tag{24}$$

$$\frac{\partial t_{ij}}{\partial v_k} = -\frac{e^{v_k}}{F(\theta_k, E_k)}\Delta s_k, \tag{25}$$

$$\frac{\partial t_{ij}}{\partial E_k} = -\frac{e^{v_k}}{F(\theta_k, E_k)^2}\frac{\partial F}{\partial E_k}\Delta s_k, \tag{26}$$

$$\frac{\partial t_{ij}}{\partial x_i} = \frac{e^{-v_k}}{F[\theta_k, E_k]}\frac{\partial \Delta s_0}{\partial x_i} \tag{27}$$

$$\frac{\partial t_{ij}}{\partial y_i} = \frac{e^{-v_k}}{F[\theta_k, E_k]}\frac{\partial \Delta s_0}{\partial y_i} \tag{28}$$

$$\frac{\partial t_{ij}}{\partial z_i} = \frac{e^{-v_k}}{F[\theta_k, E_k]}\frac{\partial \Delta s_0}{\partial z_i} \tag{29}$$

where

$$\frac{\partial F}{\partial E} = \frac{1}{2F}\{2\cos^2\theta + 2E\cos^2\theta(1 + 3\sin^2\theta)\}, \tag{30}$$

and

$$\frac{\partial \Delta s_0}{\partial x_i} = -\frac{x_{\text{r0}} - x_i}{\Delta s_0}, \tag{31}$$

$$\frac{\partial \Delta s_0}{\partial y_i} = -\frac{y_{\text{r0}} - y_i}{\Delta s_0}, \tag{32}$$

$$\frac{\partial \Delta s_0}{\partial z_i} = -\frac{z_{\text{r0}} - z_i}{\Delta s_0}, \tag{33}$$

correspond to the orientation of the tangent to the ray at the source point, $(x_{\text{r0}}, y_{\text{r0}}, z_{\text{r0}})$ being the coordinates of the first point along the ray originating from the source.

As stated previously, the model parameters for the velocity structure are defined on a relatively coarse grid (Fig. 4a), which is refined by trilinear interpolation during the computation of the forward model (Fig. 4b). Rays are traced between sources and receivers in the refined grid, where ray segment lengths are uniform and equal to the (refined) grid spacing. The wave velocity, anisotropy, phase angle and ray point coordinates are stored, and the derivatives are computed with respect to the interpolated parameters. In order to access the derivatives in the initial coarse grid, which correspond to the elements of $\mathbf{G}_n$, the derivatives obtained on the refined grid are combined using the linear interpolation coefficients used in the grid interpolation procedure (Fig. 4c). For any model parameter on the coarse grid m_j (either the horizontal wave velocity or the anisotropy parameter), we have

$$\frac{\partial g_i}{\partial m_j} = \sum_k \frac{\partial g_i}{\partial p_k}\frac{\partial p_k}{\partial m_j}, \tag{34}$$

where p_k are the model parameters on the refined grid obtained from trilinear interpolation:

$$p_k = \sum_j a_{kj}m_j, \tag{35}$$

where a_{kj} are the interpolation coefficients, so that

$$\frac{\partial p_k}{\partial m_j} = a_{kj} \tag{36}$$

and we obtain

$$\frac{\partial g_i}{\partial m_j} = \sum_k a_{kj}\frac{\partial g_i}{\partial p_k}. \tag{37}$$

3.4 Synthetic examples

In order to assess the efficiency and accuracy of the inversion method, it is first used on synthetic data sets for which the true model parameters are known. The synthetic data are generated from a 2-D heterogeneous velocity field with an average of $V_0 = 3$ mm μs^{-1} and up to 15 per cent spatial variation (from around 2.8 to 3.2 mm μs^{-1}). The full grid size is 5×5 mm^2, and the velocity is

(a) Prior model   (b) True model   (c) Inversion (mean model)
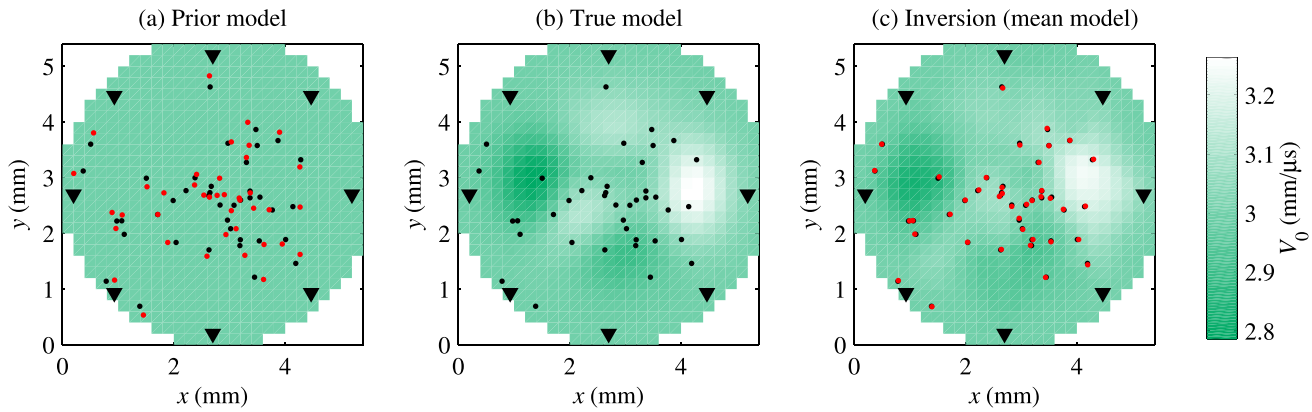
Figure 5. Synthetic example in a purely isotropic case. The initial, prior model is homogeneous and the initial AE event locations (red dots) are erroneous (a) compared to their true positions (black dots). The sensors are shown as black triangles. The true velocity model is heterogeneous with up to 15 per cent variations (b). The inverted model (c) recovered the key features of the heterogeneities as well as the even locations. Inversion parameters are reported in Table 1.

Table 1. Inversion parameters used for the 2-D synthetic test in a purely isotropic case (*) and anisotropic case (†).

Parameter	Symbol	Value
Grid refinement factor	–	10
Error on survey picks (μs)	σ_{shot}	0.01
Error on event picks (μs)	σ_{evt}	0.2
Step size	μ_n	1.0
Error on $\ln(V_0)$	σ_{v}	0.3
Error on E	σ_{E}	0.001*, 0.3†
Correlation length (mm)	λ	1.0
Error on x position (mm)	σ_{x}	0.2
Error on y position (mm)	σ_{y}	0.2
Error on z position (mm)	σ_{z}	0.2
Error on t_0 position (μs)	σ_{t0}	0.2

set to 0 outside a circular domain of 5 mm in diameter. The nominal grid spacing is 0.2 mm, and a refinement factor of 10 (grid spacing of 0.02 mm) is used in the forward computations. A set of 40 AE events are randomly positioned in the material, and eight sensors are located on the circular edge of the material. The exact arrival times are computed with the fast marching method, and a random error (±5 per cent) is added to simulate measurement uncertainty. The prior velocity structure is assumed constant, and the prior AE event locations are given by the true ones plus a random error of ±0.2 mm.

A first example is computed in a purely isotropic case, as shown in Fig. 5. The parameters used in the inversion are summarized in Table 1, and the homogeneous prior model is shown in Fig. 5(a). The quasi-Newton algorithm converges after five iterations, and least-squares residual drops by a factor of around 23 between the initial and final iterations. The result of the inversion is the 'best' solution in the sense of the least-squares norm, shown in Fig. 5(c), and corresponds to the average of all likely models once the information contained in the observations is used (Tarantola 2005). The comparison of the true model (panel b) and inverted model (panel c) reveals that the inversion procedure allows us to retrieve the main features of the true model, even though the prior model is uniform. The roughness of the inversion result is controlled by the combination of the variance σ_{v} and the correlation length λ. Increasing λ or decreasing σ_{v} reduces both the amplitude of the changes in V_0 and the length scale over which the changes are observed. In all cases, the AE event locations are retrieved almost exactly after a few iterations, despite erroneous initial locations. The average relative

error between the true and inverted locations is around 6 per cent. The improvement in the AE event locations is quite modest, and the inversion method stops converging if the *a priori* locations become too different from the true ones. This is a clear limitation of the method and limits its applicability regarding AE locations alone. However, the key benefit provided by the inversion is that we can retrieve the main features of the velocity structure.

Another example is shown in Fig. 6, where heterogeneities in both V_0 and E are implemented. The same geometrical pattern is used for velocity and anisotropy. The parameters used in the inversion are summarized in Table 1, and the homogeneous prior models are shown in Figs 6(a) and (d). Similarly to the isotropic case, the quasi-Newton algorithm converges after five iterations, and least-squares residuals drop by a factor of around 93 between the initial and final iterations. The average models resulting from the inversion procedure are shown in Figs 6(c) and (f). Again, the main features of the true model are recovered by the inversion. Because now both V_0 and E are inverted, it is important to determine whether the inversion results are correlated; in other words, it might be that jointly changing V_0 and E allows us to fit the observation equally well, in which case there would be a trade-off between these parameters. In order to estimate the posterior correlations between model parameters, we compute the posterior covariance matrix as (Tarantola 2005)

$$\widetilde{\mathbf{C}}_{\text{M}} = \left(\mathbf{G}^t \mathbf{C}_{\text{D}}^{-1} \mathbf{G} + \mathbf{C}_{\text{M}}^{-1}\right)^{-1} \tag{38}$$

and the correlation matrix as

$$\rho_{ij} = \frac{\widetilde{\mathbf{C}}_{\text{M}}^{ij}}{\sqrt{\widetilde{\mathbf{C}}_{\text{M}}^{ii}\widetilde{\mathbf{C}}_{\text{M}}^{jj}}}. \tag{39}$$

The elements of ρ corresponding to the correlations between the velocity V_0 and the anisotropy E at the same node are shown graphically in Fig. 7. All the correlations are negative, and their magnitude is relatively large (down to −0.5) where the ray coverage is poor, typically between pairs of sensors where no AE events occur. Overall, the correlations are quite small (−0.1 to −0.2), where the number of AE events is significant, such as at the centre of the model.

The synthetic tests shown here are not intended to cover all possible situations and there are known caveats associated with this exercise (Tarantola 2005; Igel 2017). Nevertheless, the overall very good match between the inversion results and the known true models gives us confidence that the method is able to retrieve the main
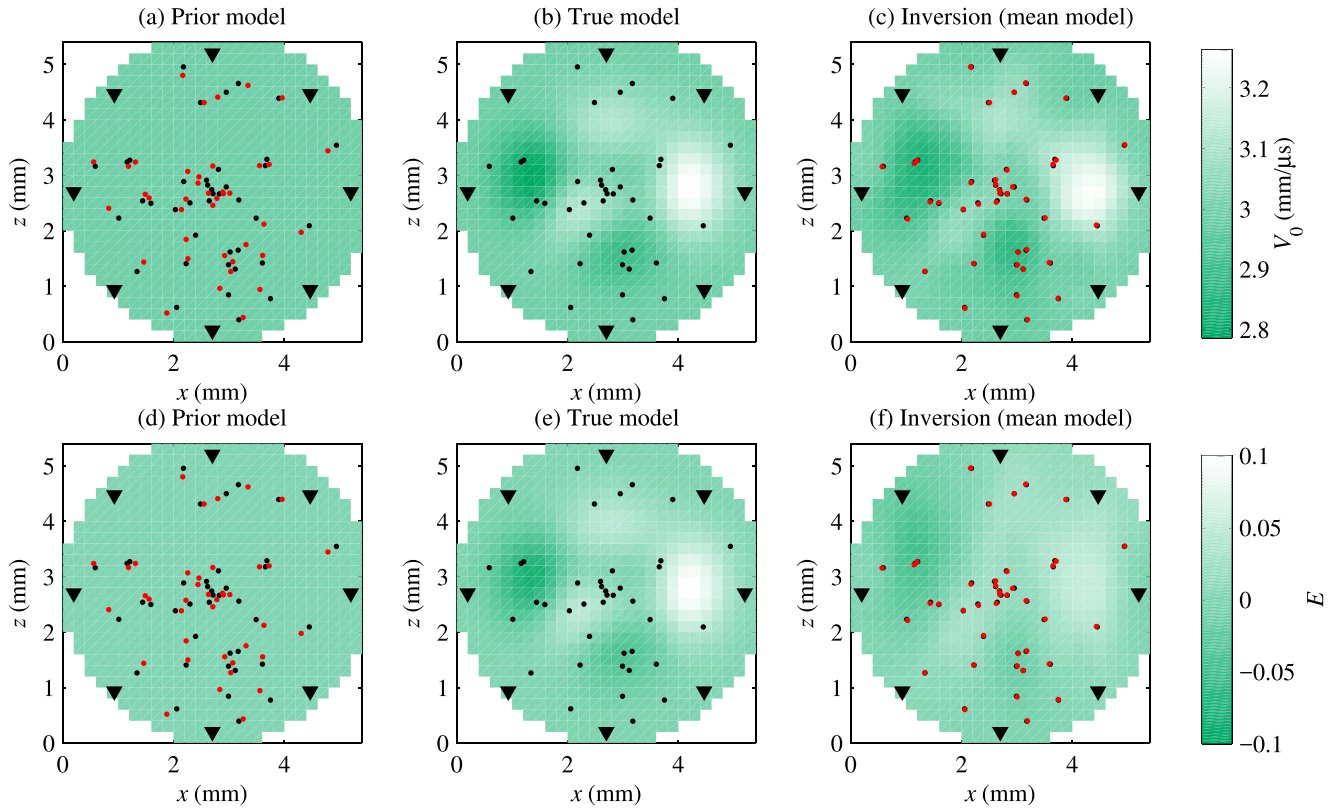
Figure 6. Synthetic example in an anisotropic case. The initial, prior model is homogeneous and the initial AE event locations (red dots) are erroneous (a) and (c) compared to their true positions (black dots). (b) and (d) The sensors are shown as black triangles. The true velocity model is heterogeneous with up to 15 per cent variation in both V_0 and E. The inverted model (c) and (f) recovered the key features of the heterogeneities as well as the even locations. Inversion parameters are reported in Table 1.
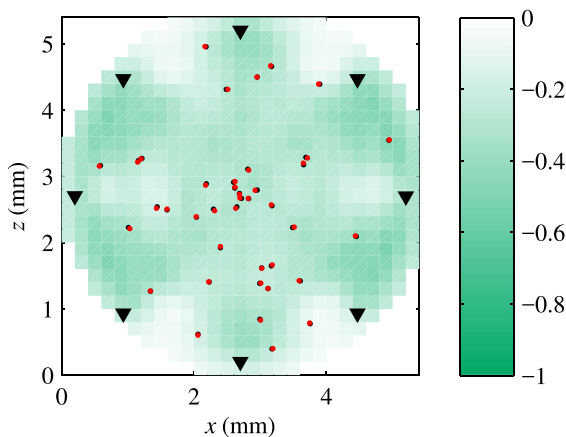
Figure 7. Correlation coefficients between the velocity V_0 and the anisotropy parameter E at each position in space.

features of the velocity structure based on AE and active measurements. The output (mean) models are spatially smooth, a feature that is entirely controlled by the variances σ_v and σ_E and the correlation length λ. The true models used here are also smooth, and the good performance of the inversion method strongly depends on the *a priori* knowledge of that smoothness, so that the variances and correlation length can be tuned to the expected variations. In practice, when working with real data, this tuning is left to the user, and any useful prior knowledge (including: signal wavelength, sample

geometry, macro- and microstructural observations and initial AE event locations) should be used to constrain the covariance matrix.

4 APPLICATION TO COMPACTION OF POROUS SANDSTONE

In order to test the tomographic method on real data and demonstrate its potential for laboratory rock deformation experiments, I perform a sequential inversion of AE and ultrasonic data obtained during a triaxial deformation experiment conducted on a porous sandstone. Sandstone is probably the ideal rock type for such an analysis because of the very large number of AE events and strong variations in wave velocity typically observed during its deformation (e.g. Fortin *et al.* 2006). Furthermore, since ultrasonic measurements can be performed repeatedly during a single experiment, if enough AE events are recorded during the time window around each active measurement, the inversion is expected to provide a complete sequence of wave velocity evolution throughout the deformation process.

In porous sandstones, the mode of deformation transitions from brittle to ductile with increasing confining pressure. Ductile deformation is initially compactant and proceeds by cataclastic flow, which is driven by microscale fracturing. While brittle deformation is always associated with localized faulting, the occurrence of strain localization during ductile deformation depends on both the initial microstructure of the rock and the stress state at which the rock is deformed (Paterson & Wong 2005; Wong & Baud 2012). In particular, a regime of compaction localization is observed at
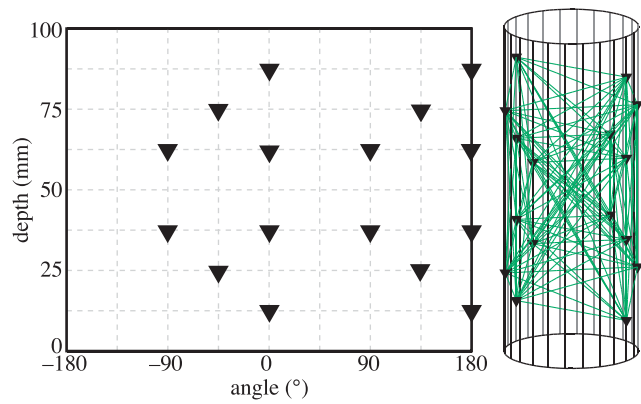
Figure 8. Sensor array geometry shown as inverted triangles as a function of angular and depth position around the sample (left) and a 3-D rendering of straight ray paths connecting all possible pairs of sensors (right).
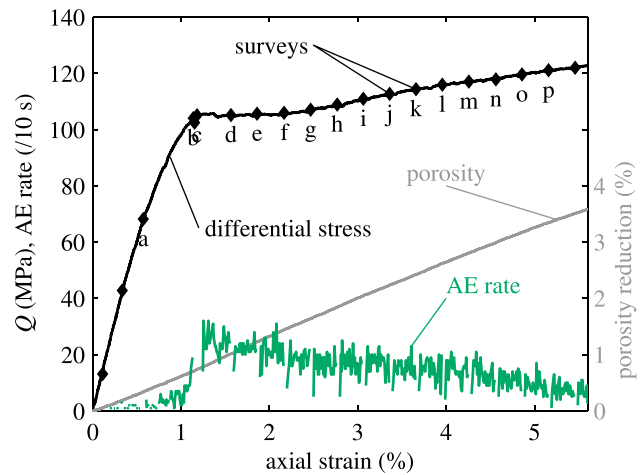

Figure 9. Differential stress (black), porosity reduction (grey) and AE rate (green) as a function of axial strain during triaxial deformation of Bleurville sandstone at 80 MPa effective confining pressure. Black diamonds indicate the points where active ultrasonic measurements were performed.

elevated confining pressures in some high porosity sandstones (e.g. Klein *et al.* 2001; Baud *et al.* 2004, 2006). The formation of compaction bands in sandstone was analysed in detail by Fortin *et al.* (2006) using AE monitoring and ultrasonic measurements, which revealed that the growth of the bands coincides with clusters of AE events and is accompanied by a progressive drop in the average wave velocity in the material. Here, I performed a triaxial deformation experiment on a sandstone similar to that used by Fortin *et al.* (2006), in the compaction banding regime. As explained in detail below, the use of AE tomography in this experiment allows us to resolve the *local* changes in wave velocity associated with the propagation of compaction bands, which was previously beyond our capabilities.

4.1 Experimental method

The rock chosen for this study is a 22 per cent porosity sandstone from Bleurville (Vosges, France). This material is composed of a majority of quartz and K-feldspar, and comes from the same area as the Bleurswiller sandstone used by Fortin *et al.* (2006). A cylinder of 40 mm in diameter was cored perpendicular to bedding, and was then cut and precision ground to 100 mm in length. The sample was inserted in a viton jacket and positioned between two steel end caps within the triaxial rock physics apparatus of the Rock and Ice Physics Laboratory at University College London (see description in Eccles *et al.* 2005).

The sample was saturated with distilled water. The confining pressure and pore pressure were set to 90 and 10 MPa, respectively, and maintained constant throughout the test by the use of servo-controlled intensifiers. The Terzaghi effective pressure was therefore equal to 80 MPa, which is well within the compactant regime for Bleurville sandstone. The pore volume change in the sample was monitored by measuring the change of fluid volume in the pore pressure intensifier with an LVDT (Linear Variable Differential Transformer) attached to the moving actuator. The axial load was measured with an external load cell and the sample shortening was measured with an external LVDT, corrected for the elastic compliance of the loading column and sample assembly. The deformation test was run at a constant strain rate of 10^{-5} s^{-1}.

The viton jacket positioned around the sample was equipped with an array of 16 piezoelectric transducers arranged in the geometry shown in Fig. 8. The piezoelectric elements of the transducers are

discs of lead–zirconate–titanate ceramic (material reference PIc255 purchased from Physik Instrumente GmbH) of 2 mm in thickness and 5 mm in diameter. These discs are mounted on top of 12 mm long aluminium inserts which act as waveguides; the additional travel-time within the waveguides was calibrated using a plain aluminium rod of known properties as the sample.

The signals from the transducers were amplified by 40 dB and recorded at 50 MHz with a digital oscilloscope (12-bit dynamic range). Passive AE monitoring was performed by recording and storing 4096 point waveforms on all channels each time a signal with an amplitude higher than 120 mV was detected on at least two channels, up to a maximum of around four events per second. The background noise level was around 20 mV. In addition, repeatedly during the experiment, active ultrasonic monitoring of the sample was performed by sending a high-frequency (1 MHz) high voltage (250 V) pulse to each transducer (then used as a source), and using the other sensors in the array to record the waveforms. Each shot was performed six times and the resulting waveforms were stacked to enhance the signal-to-noise ratio.

The waveform and amplitude spectrums of a typical AE event is shown in Fig. B1, where we observe that most of the signal is at a frequency of around 0.4 MHz. The *P*-wave velocity of the sample is of the order of 4 mm µs^{-1}, so that the wavelength of the signal is of around 1 cm. This value is four times lower than the sample diameter, and 10 times lower than the sample length.

4.2 Data analysis

The resulting mechanical data are presented in Fig. 9. The differential stress on the sample (*Q*) initially increases linearly with increasing axial strain, while the porosity also decreases. The onset of inelastic compaction is at around 45 MPa differential stress (i.e. 0.36 per cent axial strain). Beyond that point, the porosity decreases non-linearly with increasing stress. At around 1 per cent axial strain, the differential stress deviates significantly from linearity and stabilizes at around 105 MPa. The stress remains approximately constant between 1.2 and 2.2 per cent axial strain, and linear strain hardening is observed beyond that point, with the stress reaching around 120 MPa at 5.5 per cent axial strain. This mechanical behaviour

Table 2. Inversion parameters used for the sandstone compaction experiment.

Parameter	Symbol	Value
Initial grid spacing (mm)	−	5
Grid refinement factor	−	8
Error on survey picks (μs)	σ_{shot}	1
Error on event picks (μs)	σ_{evt}	2
Step size	μ_n	0.5
Error on $\ln(V_0)$	σ_v	0.12
Error on E	σ_E	0.1
Correlation length (mm)	λ	50.0
Error on x position (mm)	σ_x	2
Error on y position (mm)	σ_y	2
Error on z position (mm)	σ_z	2
Error on t_0 position (μs)	σ_{t0}	2

is typical of the ductile, compactant regime in porous sandstone (Wong & Baud 2012).

A total of 10 163 AE events were recorded during deformation. The AE rate as a function of axial strain is shown in green in Fig. 9. Based on their high amplitude and the clarity of the first arrivals, a subset of 97 740 waveforms from 6458 AE events was selected to be used in the tomographic inversion. The arrival times were initially picked automatically using a method based on an autoregressive time-series model, in which the number of autoregression coefficients was determined by the Akaike Information Criterion (Sleeman & van Eck 1999). All picks were then individually checked and corrected manually.

In addition to the AE events, active ultrasonic surveys were performed at the times marked by black diamonds in Fig. 9. The waveforms associated with an initial survey prior to deformation were picked manually, and the changes in arrival time for all subsequent surveys were computed automatically using waveform cross-correlation with subsampling at 100 MHz (Brantut *et al.* 2011; Brantut 2015). This procedure yielded a set of 147 accurate relative picks for each survey (with redundant information considering that each transducer is used as both a source and receiver sequentially).

The time-series of AE and survey data is split into 16 sequences centred around the time of each survey (labeled 'a' to 'p' in Fig. 9), leading to 16 individual data sets each containing 1 survey and from 50 (step 'a') to 625 (step 'c') AE events. The first two surveys (before 'a') were not used due to the lack of high-quality AE events. A tomographic inversion is performed for each of these data sets. The parameters used in the inversion method are summarized in Table 2. The inversion of the first data set ('a') is performed by assuming an *a priori* velocity structure that is homogeneous, anisotropic with $V_0 = 3.9$ mm μs^{-1} and $E = 0.01$. These values correspond to the average velocity model as measured by the active ultrasonic survey. The inversion of data sets 'b' to 'p' was then performed sequentially, by using the output velocity structure of the previous set as the *a priori* model for the current set. The *a priori* covariance matrix was left unchanged. In each set, the prior AE locations were set to those found with a grid search approach (with least-absolute value minimization) in the homogeneous, anisotropic velocity model as determined with the ultrasonic surveys.

4.3 Inversion results

The results of the sequential inversion procedure are summarized in Figs 10 and 11. Fig. 10 shows the spatial evolution of the relative change in horizontal velocity, computed as $(V_0 - V_0^{(a)})/V_0^{(a)}$, in a vertical slice cutting through the centre of the sample along the *x*-direction. AE hypocentre locations for each data subset are also shown on each subplot. During step (b), AEs appear quite scattered throughout the upper part of the sample, and the velocity structure is relatively homogeneous, except from a very slight anisotropy also localized at the top of the sample. By contrast, during step (c), the AE locations form a clear subhorizontal band located near the top of the sample. This clustering of AE hypocentres is accompanied with a drop of the wave velocity and an increase in anisotropy around the AE cluster. During each subsequent step from (d) to (n), the AE hypocentres form a subhorizontal front that gradually propagates from the top to the bottom of the sample. Behind the AE front, the wave velocity drops quite abruptly by 5–15 per cent and the anisotropy increases by 5–15 per cent as well, indicating that the vertical *P*-wave velocity remains almost unchanged, while the horizontal wave speed is strongly affected. During steps (o) and (p), the AEs appear less clustered and the wave velocity structure becomes more homogeneous, albeit with some scattered patches of slightly higher velocity.

As explained from the synthetic tests, the overall smoothness of the velocity structure is controlled by the combination of the variances σ_v and σ_E and the correlation length λ. The choice of a rather large λ (50 mm) was made to overconstrain the model and ensure relatively small changes between each step. Despite imposing this level of smoothness, relatively sharp transitions are observed, for instance during steps (g) and (h). This is because the inversion is performed sequentially, using the successive outputs as *a priori* models for the following steps.

Obviously, changing the *a priori* variances or correlation length would modify quantitatively the outcome of the inversion. An exploration of all possible outputs is beyond the scope of this work, but a number of tests were performed with a range of parameters (σ_v from 0.12 to 0.3, σ_E from 0.02 to 0.1 and λ from 20 to 200 mm), revealing that the pattern observed here, that is, the propagation of a front of AEs behind which the velocity drops, is retrieved systematically.

The reality of the patches of higher velocity imaged in the centre of the sample in steps (o) and (p) is difficult to confirm. The ray coverage is very poor in these areas, since all the AEs are located at the bottom of the sample and the sensors are on the sides. Hence, the active surveys do not provide enough coverage on their own to robustly determine the structure in the central part of the sample.

4.4 Significance

The combined AE locations and tomography produce an unprecedented insight into the mechanics of compaction in porous sandstone. The AE hypocentres delineate a succession of compaction bands starting at one end of the sample and systematically progressing towards the other end. Behind the compaction front, a small number of diffuse AEs are recorded. However, the tomography reveals that the material has been intensely damaged and cracked, as evidenced by the inferred large drop in horizontal wave velocity (up to 15 per cent). Here, the AEs occurring at the front have been used to image the whole sample, even in regions where little or no AE activity was recorded.

More diffuse AE activity is recorded in the last steps of deformation (o) and (p), and the tomography seems to produce a more homogeneous (anisotropic) velocity structure. The structure inferred from the last deformation step compares well with the macroscopic
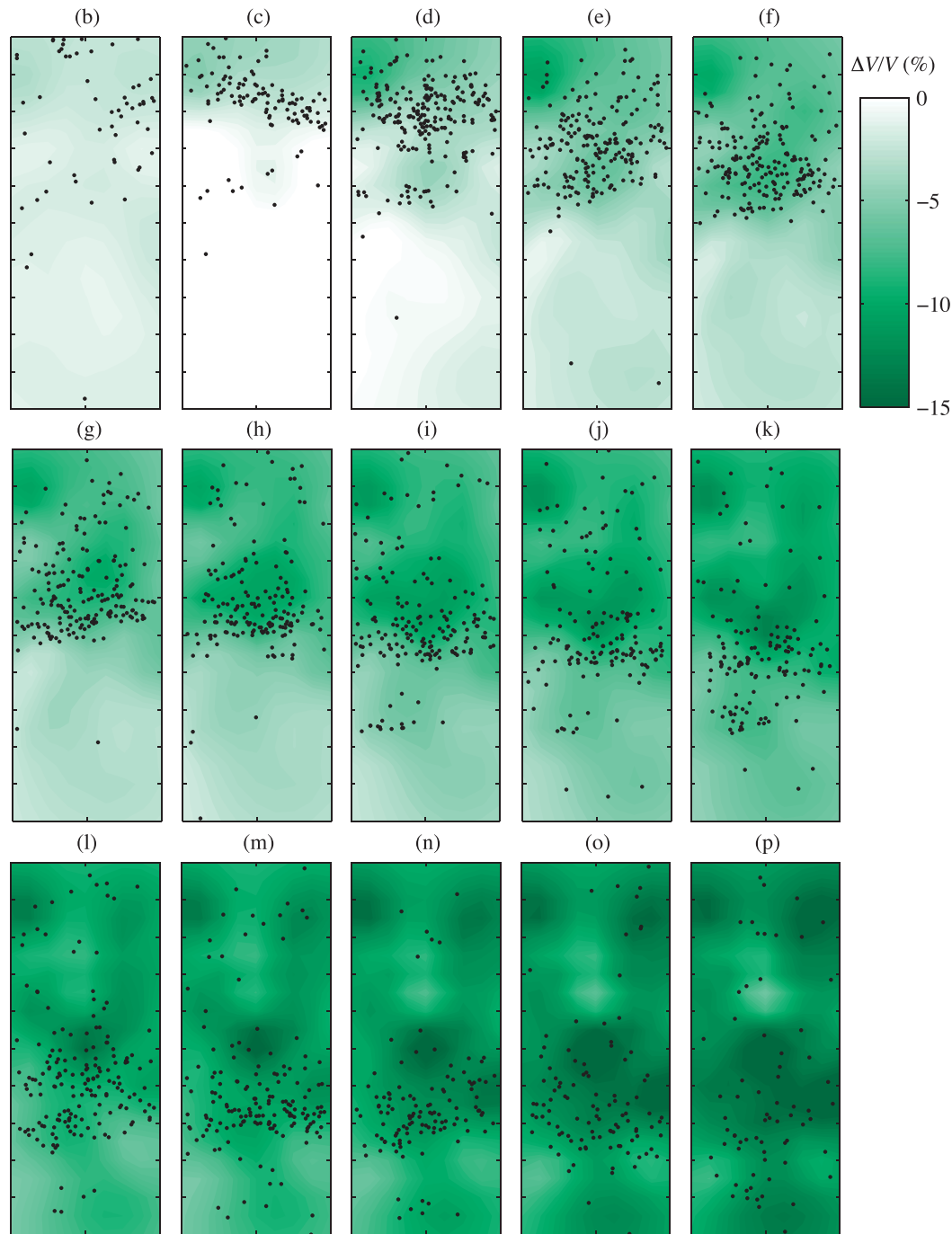
Figure 10. Sequential evolution of the horizontal *P*-wave velocity change $(V_0^{(\alpha)} - V_0^{(a)})/V_0^{(a)}$ as inferred from the inversion of each dataset (α from 'b' to 'p'). The reference velocity field is taken at step (a). All slices correspond to north–south cross-sections ((x, z) plane) running through the centre of the sample. Each slice is 40 mm in width and 100 mm in height, which matches the initial sample dimensions. The black dots correspond to the AE event hypocentres located within $|y| \leq 2.5$ mm of the central section of the sample.

picture of the deformed sample recovered after unloading and de-compression, as well as with the total number of AEs recorded in the sample, shown in Fig. 12.

These results imply that the accumulated AE density is correlated with the horizontal *P*-wave velocity drop. This is consistent with the idea that each AE corresponds to the propagation of one or several subvertical microcracks, which in turn are known to dramatically affect the wave velocity of the material (e.g. Sayers & Kachanov

1995). The correlation between the local cumulative AE number and the change in wave velocity is shown graphically in Fig. 13. There is a clear proportionality between the maximum AE number in a given location and the corresponding velocity change at that location. However, for a given velocity change, the cumulative AE number can be significantly less than the potential maximum, as evidenced by the spreading of the points along the *y*-axis in Fig. 13. The lack of direct proportionality between wave velocity change and AE
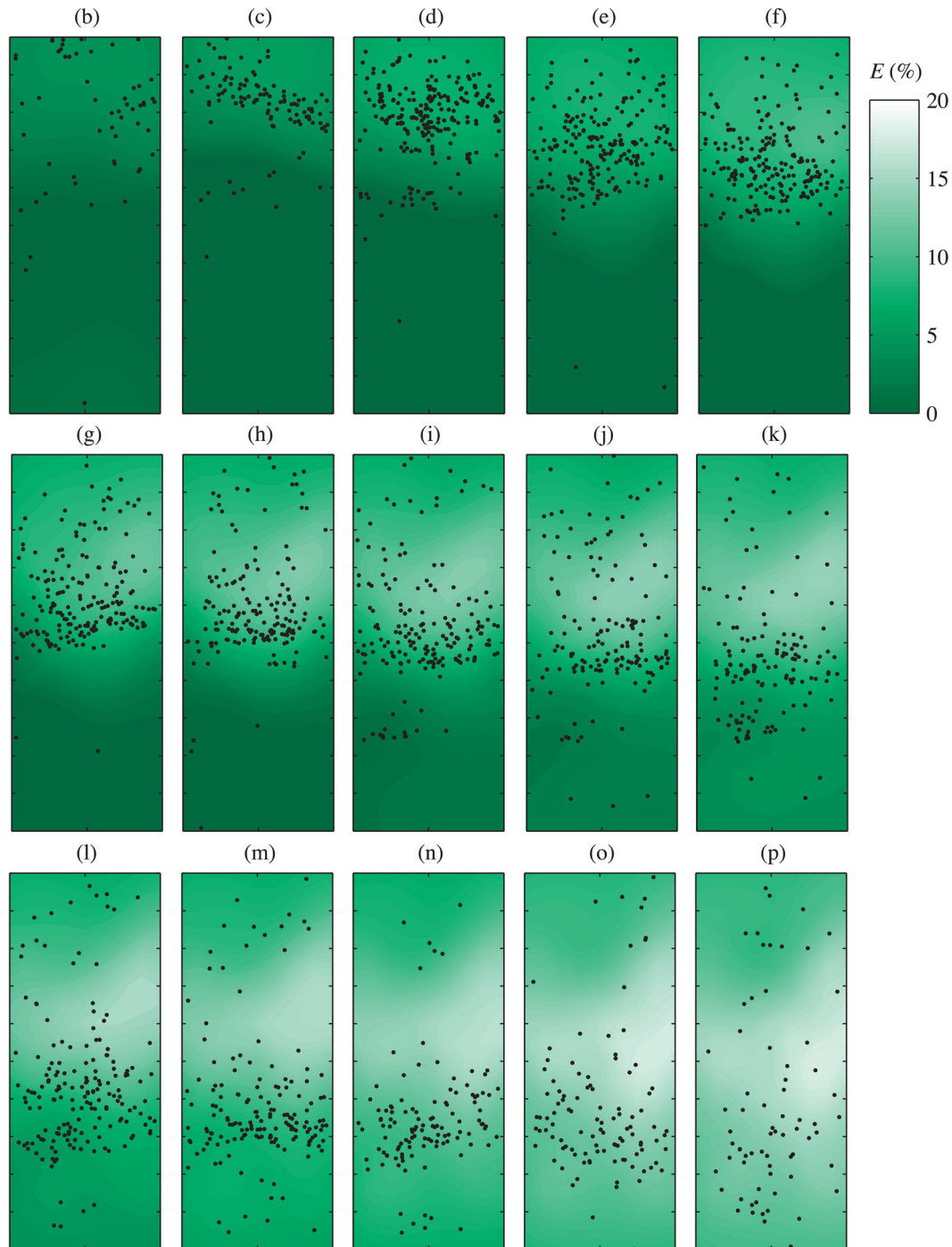
Figure 11. Evolution of the anisotropy parameter *E* during deformation, as inferred from the inversion of data sets (a)–(p). All slices correspond to north–south cross-sections ((x, z) plane) running through the centre of the sample. Each slice is 40 mm in width and 100 mm in height, which matches the initial sample dimensions. The black dots correspond to the AE event hypocentres located within $|y| \leq 2.5$ mm of the central section of the sample.

count—the correlation being only with the *maximum* AE count—is maybe an artefact arising from the AE detection and selection thresholds, but clearly highlights the potential of the tomographic method to image areas where no AEs are recorded but are still heavily microcracked.

The progression of the compaction front imaged by AE tomography is a key element to understand the mechanical behaviour of the rock. Throughout the propagation of the front, from steps (b)

to (h), the applied differential stress remains constant (Fig. 9). The front seems to stagnate from steps (h) to (l), which corresponds to a period of slight strain hardening. Beyond step (l), the front seems to propagate further while losing its coherence, which corresponds to a decrease in strain hardening. During this stage, the whole sample becomes cracked and the wave velocity becomes again more homogeneous. During steps (h)–(l), the rock is effectively a bimaterial, with the top half heavily cracked and mostly incohesive, and
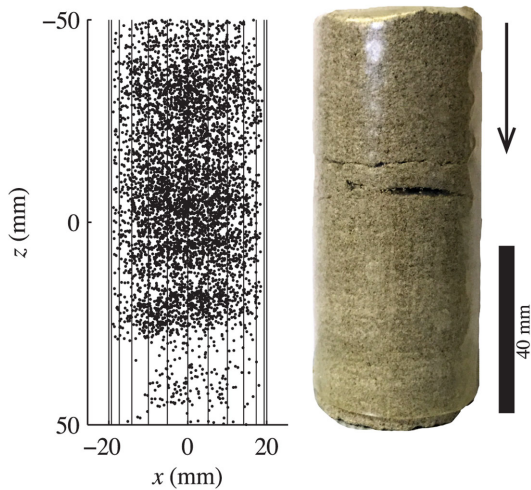
Figure 12. AE hypocentres observed during the full deformation process (left), and photograph of the deformed sample, jacketed in a transparent heatshrink sleeve (right). The arrow indicates the direction of propagation of the compaction front.
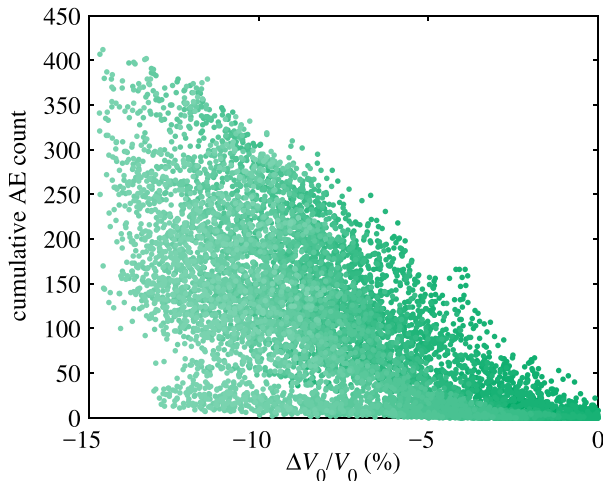
Figure 13. Cumulative AE number as a function of the relative change in horizontal *P*-wave velocity. Each dot corresponds to the AE count and the average velocity change in a cubic volume of $10 \times 10 \times 10$ mm^3. Colours from dark to light green correspond to time windows (b)–(o).

the bottom half more or less intact. The period of strain hardening indicates that the deformation of the top half requires progressively more stress to proceed [strain hardening is a common observation in the ductile cataclastic flow regime, see Wong *et al.* (1997)]. The subsequent progression of the compaction front in the bottom half of the sample, together with the slight decrease in strain hardening, shows that it becomes more energetically favourable to start compacting the intact part of the rock rather than continue deforming part the damaged part of the sample.

Overall, the tomographic imaging reveals a close relationship between AE locations and density, changes in *P*-wave velocity and compaction localization in the sample. In a previous study by Fortin *et al.* (2006) on a similar rock, AE locations were used to image the growth of compaction bands and the relationships between compaction bands and pre-existing heterogeneities in the sample. In that study, compaction bands initiated at various locations within the sample and did not start specifically at one end of the sample.

By contrast, here we find that compaction bands successively form next to each other from the top to the bottom of the sample. This key difference in deformation mode might be associated with the lack of pre-existing heterogeneities in our sample compared to that used by Fortin *et al.* (2006). This explanation is consistent with the initiation of compaction near the end of the sample, where the stress state is slightly more compressive due to frictional effects between the sample and the end-caps: this stress heterogeneity is the dominant one compared to other microstructural heterogeneities in the sample.

5 CONCLUSIONS

In this paper, I have presented a method that combines active ultrasonic monitoring and passive AE recording in laboratory samples to perform 3-D, anisotropic wave velocity tomography. The method is analogous to Local Earthquake Tomography, pioneered by Aki & Lee (1976) and Thurber (1983). The data used are arrival times from both active sources with known positions and passive sources with unknown positions. The model parameters are the wave velocities at regular gridpoints within the sample (a horizontal *P*-wave speed V_0 and an anisotropy parameter *E*, in an elliptic VTI model) and AE event locations. The forward problem is solved efficiently by the fast marching method (e.g. Sethian 1999). The inverse problem is solved with the quasi-Newton method (Tarantola 2005).

Tests performed using synthetic data with noise indicate a good performance of the method, with rapid convergence and good agreement between the inversion results and the true input model. The results are somewhat less accurate when performing inversion with anisotropy, and there are small negative correlations between the inverted wave velocity and anisotropy parameters. These problems are inherent to all tomographic methods and can only be circumvented by using better constraints on prior models and covariances.

The application of the method to experimental data obtained during compaction of a porous sandstone reveal unprecedented information on the relationships between strain localization, AE density and changes in wave velocity. The tomographic imaging shows very clearly the propagation of a compaction front, highlighted by clusters of AE events, and leaving a heavily damaged material behind (with drops in horizontal *P*-wave velocity of up to 15 per cent). These results are consistent with the post-mortem structure of the sample.

The largest source of error in the approach is, by far, the lack of accuracy of the *P*-wave arrival picks on passive AE records. Here, all the picks were manually checked, but this task would be near impossible on very large data sets (or, rather, not considered a good use of people's time). One way to improve this crucial step would be to use machine learning techniques to automate the picking and provide individual measures of picking errors for each arrival time. These individual errors could then be used to fill the data covariance matrix and obtain more robust inversion results.

The overall good performance of the method on real laboratory data demonstrates the potential of AE tomography as a routine *in situ* imaging technique. Indeed, the method requires only arrival time data from AE transducers, which are already routinely collected in several laboratories. It is therefore imaginable to revisit pre-existing data sets and produce new complementary results with AE tomography. To this end, I provide the full software suite FaATSO online with the required documentation and manuals (https://github.com/nbrantut/FaATSO.git), with the hope of

encouraging the development and use of improved AE tomography techniques.

REFERENCES

Aki, K. & Lee, W.H.K., 1976. Determination of three-dimensional velocity anomalies under and seismic array using first P arrival times from local earthquakes. 1. A homogeneous initial model, *J. geophys. Res.,* **81**(23), 4381–4399.

Baud, P., Klein, E. & Wong, T.-F., 2004. Compaction localization in porous sandstones: spatial evolution of damage and acoustic emission activity, *J. Struct. Geol.,* **26**, 603–624.

Baud, P., Vajdova, V. & Wong, T.-F., 2006. Shear-enhanced compaction and strain localization: inelastic deformation and constitutive modeling of four porous sandstones, *J. geophys. Res.,* **111**, B12401, doi:10.1029/2005JB004101.

Brantut, N., 2010. Thermo-hydro-mechanical and chemical couplings during nucleation and seismic slip: experiments and theory, *PhD thesis,* Université Paris Diderot.

Brantut, N., 2015. Time-dependent recovery of microcrack damage and seismic wave speeds in deformed limestone, *J. geophys. Res.,* **120**(12), 8088–8109.

Brantut, N., Schubnel, A. & Guéguen, Y., 2011. Damage and rupture dynamics at the brittle-ductile transition: the case of gypsum, *J. geophys. Res.,* **116**, B01404, doi:10.1029/2010JB007675, 2011.

Brantut, N., Heap, M.J., Baud, P. & Meredith, P.G., 2014. Rate- and strain-dependent brittle deformation of rocks, *J. geophys. Res.,* **119**, doi:10.1002/2013JB010448.

Dines, K.A. & Lytle, R.J., 1979. Computerized geophysical tomography, *Proc. IEEE,* **67**(7), 1065–1073.

Eccles, D., Sammonds, P.R. & Clint, O.C., 2005. Laboratory studies of electrical potential during rock fracture, *Int. J. Rock Mech. Min. Sci.,* **42**(7–8), 933–949.

Falls, S.D., Young, R.P., Carlson, S.R. & Chow, T., 1992. Ultrasonic tomography and acoustic emission in hydraulically fractured Lac du Bonnet grey granite, *J. geophys. Res.,* **97**(B5), 6867–6884.

Fortin, J., Stanchits, S., Dresen, G. & Guéguen, Y., 2006. Acoustic emission and velocities associated with the formation of compaction bands in sandstone, *J. geophys. Res.,* **111**, B10203, doi:10.1029/2005JB003854.

Fortin, J., Stanchits, S., Dresen, G. & Guéguen, Y., 2009. Acoustic emissions monitoring during inelastic deformation of porous sandstone : comparison of three modes of deformation, *Pure appl. Geophys.,* **66**, 823–841.

Fukushima, Y., Nishizawa, O. & Sato, H., 2009. A performance study of laser doppler vibrometer for meauring waveforms from piezoelectric transducers, *IEEE Trans. Ultrason. Ferroelectr. Freq. Control,* **56**(7), 1442–1450.

Gupta, I.N., 1973. Seismic velocities in rock subjected to axial loading up to shear fracture, *J. geophys. Res.,* **78**(29), 6936–6942.

Igel, H., 2017. *Computational Seismology,* Oxford University Press, Oxford, UK.

Jansen, D.P., Carlson, S.R., Young, R.P. & Hutchins, D.A., 1993. Ultrasonic imaging and acoustic emission monitoring of thermally induced microcracks in Lac du Bonnet granite, *J. geophys. Res.,* **98**(B12), 22 231–22 243.

Klein, E., Baud, P., Reuschlé, T. & Wong, T.-F., 2001. Mechanical behaviour and failure mode of Bentheim sandstone under triaxial compression, *Phys. Chem. Earth (A),* **26**(1–2), 21–25.

Lockner, D. & Byerlee, J., 1977. Acoustic emission and creep in rock at high confining pressure and differential stress, *Bull. seism. Soc. Am.,* **67**(2), 247–258.

Lockner, D.A., 1993. Room temperature creep in saturated granite, *J. geophys. Res.,* **98**(B1), 475–487.

Lockner, D.A., Byerlee, J.D., Kuksenko, V., Ponomarev, A. & Sidorin, A., 1992. Observation of quasistatic fault growth from acoustic emissions, in *Fault Mechanics and Transport Properties of Rocks,* pp. 3–31, eds Evans, B. & Wong, T.F., International Geophysics Series, Academic Press, London.

Mogi, K., 1968. Source locations of elastic shocks in the fracturing process in rocks (1), *Bull. Earthq. Res. Inst.,* **46**, 1103–1125.

Nishizawa, O., Onai, K. & Kusunose, K., 1984. Hypocenter distribution and focal mechanism of ae events during two stress stage creep in Yugawara andesite, *Pure appl. Geophys.,* **122**, 36–52.

Paterson, M.S. & Wong, T.F., 2005. *Experimental Rock Deformation—The Brittle Field,* 2nd edn, Springer-Verlag, Berlin Heidelberg.

Rawlinson, N. & Sambridge, M., 2003. Seismic traveltime tomography of the crust and lithosphere, *Adv. Geophys.,* **46**, 81–197.

Rickett, J. & Fomel, S., 1999. A second-order fast marching eikonal solver, *Stanford Explor. Proj. Rep.,* **100**, 287–293.

Rouy, E. & Tourin, A., 1992. A viscosity solutions approach to shape-from-shading, *SIAM J. Numer. Anal.,* **29**(3), 867–884.

Sanderson, C. & Curtin, R., 2016. Armadillo: a template-based C++ library for linear algebra, *J. Open Source Softw.,* **1**(2), 26–32.

Sayers, C. & Kachanov, M., 1995. Microcrack-induced elastic wave anisotropy of brittle rocks, *J. geophys. Res.,* **100**(B3), 4149–4156.

Scholz, C.H., 1968. Experimental study of the fracturing process in brittle rocks, *J. geophys. Res.,* **73**(4), 1447–1454.

Schubnel, A., Nishizawa, O., Masuda, K., Lei, X.J., Xue, Z. & Guéguen, Y., 2003. Velocity measurements and crack density determination during wet triaxial experiments on Oshima and Toki granites, *Pure appl. Geophys.,* **160**, 869–887.

Sethian, J.A., 1999. Fast marching methods, *SIAM Rev.,* **41**(2), 199–235.

Sethian, J.A. & Vladimirsky, A., 2003. Ordered upwind methods for static Hamilton-Jacobi equations: theory and algorithms, *SIAM J. Numer. Anal.,* **41**(1), 325–363.

Sleeman, R. & van Eck, T., 1999. Robust automatic P-phase picking: an on-line implementation in the analysis of broadband seismogram recordings, *Phys. Earth planet. Inter.,* **113**, 265–275.

Tang, X.M., Zhu, Z. & Toksöz, M.N., 1994. Radiation patterns of compressional and shear transducers at the surface of an elastic half-space, *J. acoust. Soc. Am.,* **95**(1), 71–76.

Tarantola, A., 2005. *Inverse Problem Theory,* 2nd edn, Society for Industrial Mathematics, Philadelphia.

Thomsen, L., 1986. Weak elastic anisotropy, *Geophysics,* **51**(10), 1954–1966.

Thurber, C.H., 1983. Earthquake locations and three-dimensional crustal structure in the Coyote Lake area, central California, *J. geophys. Res.,* **88**(B10), 8226–8236.

Tsai, Y.-H.R., Cheng, L.-T., Osher, S. & Zhao, H.-K., 2003. Fast sweeping algorithms for a class of Hamilton-Jacobi equations, *SIAM J. Numer. Anal.,* **41**(2), 673–694.

Wong, T.-F. & Baud, P., 2012. The brittle-ductile transition in porous rock: a review, *J. Struct. Geol.,* **44**, 25–53.

Wong, T.F., David, C. & Zhu, W., 1997. The transition from brittle faulting to cataclastic flow in porous sandstones: mechanical deformation, *J. geophys. Res.,* **102**(B2), 3009–3025.

Yoshimitsu, N., Furumura, T. & Maeda, T., 2016. Geometric effect on a laboratory-scale wavefield inferred from a three-dimensional numerical simulation, *J. appl. Geophys.,* **132**, 184–192.

Yukutake, H., 1989. Fracturing process of granite inferred from measurements of spatial and temporal variations in velocity during triaxial deformations, *J. geophys. Res.,* **94**(B11), 15 639–15 651.

APPENDIX A: ANISOTROPY AND THE FAST MARCHING METHOD

The fast marching method was developed to solve a general class of Hamilton–Jacobi equations:

$$H(\mathbf{x}, \mathbf{p}) = s(\mathbf{x}), \tag{A1}$$

where H is a Hamiltonian operator and $\mathbf{p}$ a vector of its arguments. The eikonal equation is a special case of (A1) where $\mathbf{p} = \nabla u$ and s is the slowness. The conventional algorithm of the fast marching method outlined in Section 2 applies when the Hamiltonian H satisfies the so-called Osher's criterion (see for instance a description in Tsai *et al.* 2003):

$$p_i \frac{\partial H}{\partial p_i} \geq 0, \tag{A2}$$

where the p_i denote the elements of the vector $\mathbf{p}$. In the case of a VTI material with elliptical anisotropy, as described by eq. (5), the Hamiltonian is of the form:

$$H(p_1, p_2, p_3) = V_0 \sqrt{p_1^2 + p_2^2 + p_3^2} \left(1 + E p_3^2 / (p_1^2 + p_2^2 + p_3^2)\right), \tag{A3}$$

and satisfies Osher's condition provided that $-1/2 < E < 1$.

APPENDIX B: EXAMPLE AE WAVEFORM AND SPECTRUM

Fig. B1 shows a representative example of the raw waveform (top) and the amplitude spectrum (bottom) of an AE event recorded during the sandstone compaction experiment. The spectrum shows that the signal is dominated by frequencies up to 0.4 MHz, which corresponds to a wavelength of the order of 1 cm.
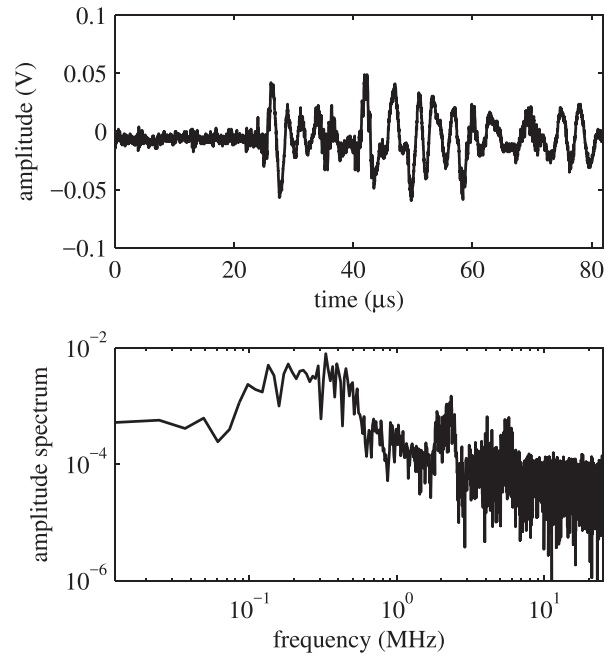
Figure B1. Representative example of a raw AE waveform (top) and its amplitude spectrum (bottom).